

MIT Open Access Articles

High-performance MEMS square electrode quadrupole mass filters for chip-scale mass spectrometry

The MIT Faculty has made this article openly available. **Please share** how this access benefits you. Your story matters.

Citation: Cheung, Kerry, Luis F. Velasquez-Garcia, and Akintunde I. Akinwande. "High-performance MEMS Square Electrode Quadrupole Mass Filters for Chip-scale Mass Spectrometry." IEEE, 2010. 867–870. Web. 4 Apr. 2012. © 2010 Institute of Electrical and Electronics Engineers

As Published: <http://dx.doi.org/10.1109/MEMSYS.2010.5442344>

Publisher: Institute of Electrical and Electronics Engineers (IEEE)

Persistent URL: <http://hdl.handle.net/1721.1/69930>

Version: Final published version: final published article, as it appeared in a journal, conference proceedings, or other formally published context

Terms of Use: Article is made available in accordance with the publisher's policy and may be subject to US copyright law. Please refer to the publisher's site for terms of use.



HIGH-PERFORMANCE MEMS SQUARE ELECTRODE QUADRUPOLE MASS FILTERS FOR CHIP-SCALE MASS SPECTROMETRY

Kerry Cheung, Luis F. Velásquez-García, and Akintunde I. Akinwande
Massachusetts Institute of Technology, USA

ABSTRACT

We report exciting experimental data from a low-cost, high-performance square electrode quadrupole mass filter with integrated ion optics intended for chip-scale mass spectrometry. The device showed a mass range of 650 amu and a maximum resolution of ~ 80 , metrics that are comparable to the state-of-the-art. We demonstrated that operating our device in the second stability region leads to higher performance despite the unconventional electrode geometry. The data also suggests ion behavior that deviates from the standard circular rod case, motivating new studies.

INTRODUCTION

Mass spectrometers are powerful analytical tools that have a wide range of applications spanning national security, industrial processing, space exploration, environmental monitoring, healthcare, and others. In recent years, there has been a growing desire to take these instruments into the field to perform on-site analyses. To achieve this move, mass spectrometers need to be smaller, lighter, more robust, and low-powered. Miniaturization addresses most of these issues by achieving portability through reducing size and weight. The smaller devices will enable operation at higher pressures, relaxing the need for large, heavy, and power-hungry vacuum pumps [1], [2].

The four major components of a mass spectrometer are the ionizer, the mass filter, the detector, and the pump. The ionizer places a charge on the compound to be analyzed, the mass filter sorts these ions by their mass-to-charge ratios (m/e), the detector counts the number of ions that pass through the mass filter, and the pump keeps the system under vacuum. If the m/e to be filtered is varied with time, the resulting plot of the detected signal is called a mass spectrum. To date, these components have all been scaled-down in one form or another by utilizing conventional machining technologies. Despite the performance achieved, the construction methodology is relatively expensive, thus limiting the widespread adoption of this tool.

Miniaturization with microelectromechanical systems (MEMS) technology has recently received significant attention [3]-[5]. The economies of scale that come with microfabrication leads to lowered costs, while the associated precision and potential for component

integration holds the promise of high-performance systems. The highly repeatable nature of completely batch-fabricated devices will also provide additional cost savings since each component will not require individual characterization. If these systems become sufficiently low-cost, chip-scale mass spectrometers will become a commodity item.

Many of the MEMS miniaturization efforts have been focused around the mass filter component. The quadrupole mass filter (QMF) has been quite popular due to its simplicity, versatility, and well understood physics of operation [6]. Impressive work on MEMS-based QMFs has been reported but they all required some degree of post-fabrication electrode assembly [7]-[9]. The assembly methodologies presented lead to electrode-to-housing misalignments and increased costs. Electrode misalignments limit the maximum performance that can be achieved, while the assembly step serves as a bottleneck to mass production. Previously, we presented a new class of chip-scale QMFs that addressed these issues and demonstrated a proof-of-concept device that utilized square electrode geometry [10]. In this paper, we introduce the design concept followed by the improved fabrication process flow. New experimental data will then be provided and their implications discussed.

DESIGN AND FABRICATION

In most commercially available QMFs, the electrodes are cylindrical rods instead of the ideal hyperbolic ones due to the increased manufacturing simplicity. Cylindrical electrodes were used in the other MEMS-based QMFs but it required post-fabrication assembly. Creating the cylindrical geometry in the plane of the wafer is not readily feasible with well-established microfabrication techniques so we proposed using square electrode geometry instead [10]. This concept is an extension of the cylindrical rod approximation used for conventional devices. It works because QMF operation is a boundary value problem in which the electric fields established by the various electrode geometries are very similar near the central axis of the device. The central region is where transmitted ions spend a significant portion of their flight times so we expect proper mass filtering to occur.

Fig. 1 shows a cross-sectional schematic of our QMF detailing the design concept. The electrodes, ion

optics, and housing are integrated into a monolithic block. The device is comprised only of heavily-doped silicon and silicon dioxide, making the structure more thermally and mechanically robust than the other MEMS-based QMFs. More importantly, this design concept can be readily extended to implement more advanced architectures such as inclusion of pre-filters, complex ion optics, and even tandem quadrupoles.

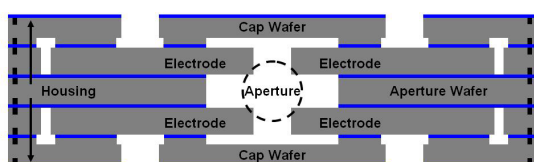


Figure 1. Schematic of device cross-section. The electrodes are electrically isolated from the housing and cap wafers by thick thermal oxide.

The device is comprised of five double-side polished silicon wafers that were heavily doped with antimony to ensure similar behavior to a metal. All five wafers began with the same processing. Alignment marks were placed on both sides, followed by a 2.5 μm wet oxidation, and a 250 nm low-pressure chemical vapor deposition (LPCVD) of silicon-rich silicon nitride. The nitride was used to protect the bond interfaces throughout subsequent process steps.

The cap wafers and aperture wafer were processed in a similar manner. Thick resist was spun on both sides followed by double-sided contact photolithography. The exposed nitride and oxide were removed using a two-step reactive ion etch (RIE), followed by a deep reactive ion etch (DRIE) to pattern the silicon on both sides. The cap wafers had a shallow trench on the front-side and a through-wafer etch on the back-side to produce the contact vias. The aperture wafer had the same halo pattern etched to the same depth on both sides to ensure symmetry.

The electrode wafers began with double-sided photo of the same pattern. The exposed nitride and thermal oxide were removed using RIE. The wafers then had 1.4 μm of nitride deposited on one side with plasma-enhanced chemical vapor deposition (PECVD) to serve as a timed-etch mask. The processed cap wafers and the electrode wafers were placed into phosphoric acid for 1.5 hours to remove all the nitride on the cap wafers while leaving ~ 150 nm of LPCVD nitride on one side of the electrode wafers. The wafers were cleaned and aligned so the shallow trench on the cap wafers would contact the nitride-free surface of the electrode wafers. The two wafer pairs were fusion bonded with compression at 2500 N for 12+ hours, followed by a 1 hour anneal in nitrogen at 1000 $^{\circ}\text{C}$. The cap/electrode stacks then had thick photoresist spun on the face with LPCVD nitride and the pattern

for the electrodes and lens elements were transferred. The exposed nitride and oxide were removed, and the electrodes and lens elements were defined with DRIE.

The two cap/electrode stacks and the aperture wafer were all placed into phosphoric acid for 1.5 hours to remove all the remaining nitride. The wafers were cleaned and fusion bonded with the aperture wafer sandwiched between the cap/electrode stacks. The final 5-wafer stack was die-sawed to separate the devices while opening the inlet and outlet. A solvent ultrasonic clean was used after this step to alleviate shorting issues encountered from die-saw particles.

EXPERIMENTAL RESULTS

Characterization of the quadrupole was carried out in an in-house testing facility. The device was held in a custom-made vacuum flange mount that also held a Channeltron[®] electron multiplier that served as the detector, a Slim-Line[®] ionizer, and stainless steel ion lenses. The assembled flange was placed onto a vacuum system that can reach a base pressure of 1×10^{-8} Torr. Perfluorotributylamine (FC-43), Argon, or air was introduced to a pressure of $\sim 3 \times 10^{-5}$ Torr before any mass spectra were taken. The measured signal from the detector was amplified through a low-noise preamplifier and collected through a DAQ card to produce the mass spectrum.

The r.f. component of the drive signal originates from a function generator that sets the frequency and initial maximum amplitude. During scanning, the amplitude is modulated by a control voltage from the DAQ card. The signal then passes a wide-band amplifier and an air-core transformer. This step splits the r.f. into two components that are 180 $^{\circ}$ out of phase and steps-up the voltage. The d.c. drive components stem from the DAQ card and is amplified by op-amps set in a non-inverting amplifier configuration. The increased d.c. voltages are then combined with the r.f. components at the transformer center-tap to produce the necessary drive signals. The DAQ card interfaces with a PC and custom LabVIEW program that sets the operation conditions, scans the r.f. and d.c. voltages, acquires the detected signal, and generates the spectrum.

Validation of Ion Optics

The integrated lenses were initially grounded so the voltages on the stainless steel optics and the ionizer could be optimized first. Once a good mass spectrum was obtained, the integrated inlet lens elements had their voltages varied. In Fig. 2, we can clearly see enhanced transmission when the inlet voltage was set to -3 Volts. The same effect was demonstrated during operation in the second stability region (SSR), validating that unconventional lens geometry can be used to improve device performance. The integrated

exit lens was grounded due to shorting issues but a functional one would lead to further increases in transmission.

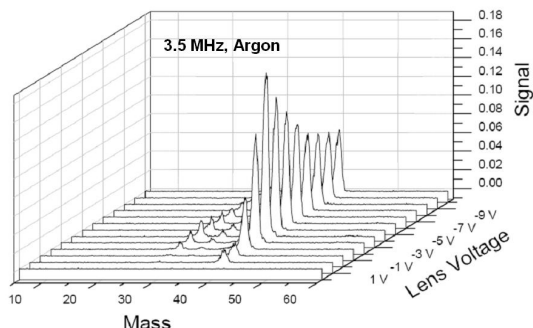


Figure 2. Transmitted signal versus inlet lens voltage for Argon with trace air at 3.5 MHz in the first stability region.

Maximum Mass Range

FC-43 was used as the analyte due to its high-mass peaks. At 1.8 MHz, we demonstrated a mass range of 650 amu. In Fig. 3, we see a peak-width of 3.6 amu and 6.5 amu at mass 69 and mass 131 respectively, corresponding to a resolution of ~ 20 . A peak-width of 7.8 amu and 9.8 amu was obtained at mass 219 and mass 264 respectively, indicating a resolution of ~ 28 . The increase in resolution was most likely a result of non-linearity in the r.f. amplifier.

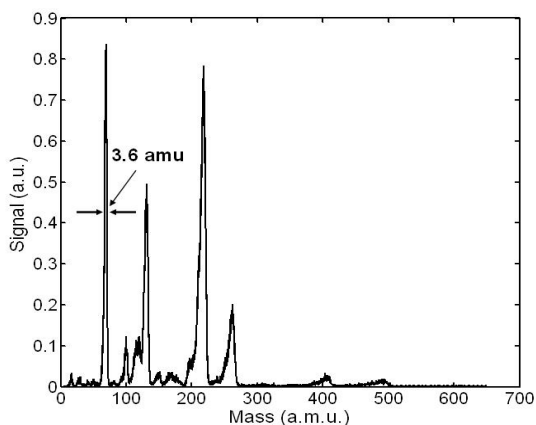


Figure 3. Mass spectrum for perfluorotributylamine (FC-43) at 1.8 MHz in the first stability region.

Minimum Peak-Width

For this experiment, the device was driven at 4.0 MHz and the analyte was Argon. In Fig. 4, we can see the peak for Argon at mass 40 as well as peaks at mass 28 and mass 32. The appearance of Nitrogen and Oxygen was due to a trace leakage of air into our Argon line. We demonstrated a peak-width of 1.0 amu at mass 40 and a peak-width of 0.7 amu at mass 28, both corresponding to a resolution of ~ 40 . We can also see the existence of precursor peaks on the low-

mass side of the detected peaks. These undesirable artifacts are a direct result of the non-ideal, higher-order terms associated with our device geometry [6]. The electric potential of our QMF can be expressed as the multipole expansion [11]:

$$\Phi = \Phi_0 \sum_n C_n \cos(n\theta) \left(\frac{r}{r_0} \right)^n \quad n = 2, 6, 10, 14 \dots \quad (1)$$

where Φ_0 is the drive signal, r is the distance from the central axis, and r_0 is the device radius. Unlike the circular rod case, the higher-order components of our device are substantially more dominant with respect to the ideal quadrupole term C_2 (Table 1).

Table 1. Multipole expansion coefficients for optimized quadrupole electrode geometries.

	Circular Rods	Square Electrodes
C_2	1.0016e0	0.7838e0
C_6	1.200e-3	8.0909e-2
C_{10}	-2.4325e-3	3.2235e-2
C_{14}	-2.6928e-4	1.8101e-2

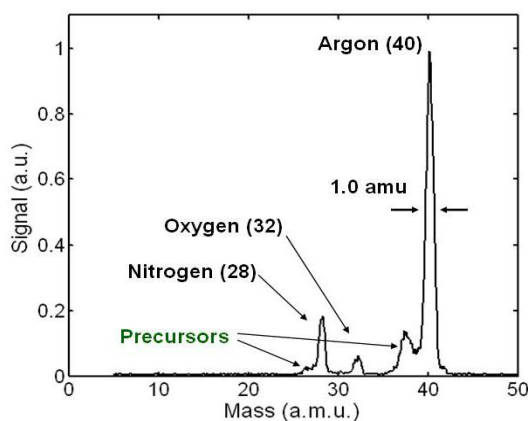


Figure 4. Mass spectrum for Argon with trace air at 4.0 MHz in the first stability region with precursors.

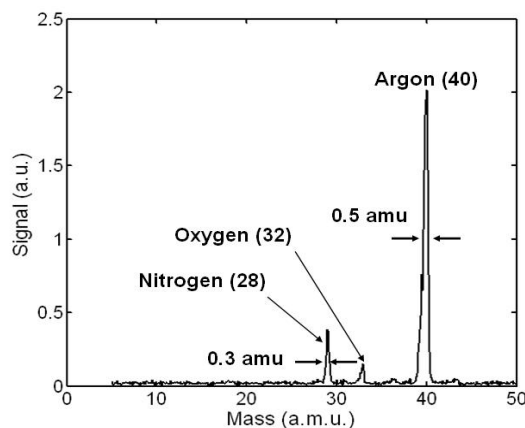


Figure 5. Mass spectrum for Argon with trace air at 2.0 MHz in the second stability region.

The device was also driven at 2.0 MHz in the SSR. In Fig. 5, we show a peak-width of 0.5 amu at mass 40 corresponding to a resolution of ~ 80 . We doubled resolution despite operating at half the frequency. Utilizing the SSR effectively enhances the filtering mechanism leading to increased resolution at the expense of transmission. We can also see that the precursor peaks were removed, drastically improving the peak-shape. This result shows that operating our device in the SSR is a viable method for addressing degradations in performance associated with using the square geometry.

Ultimate Resolution

To probe the ultimate resolution of our device, we increased the Mathieu parameter a in the software until the main peak in the spectrum nearly disappears. For various frequencies, ion energies, and analytes, the ultimate resolution was determined in this manner. We found the corner of the first stability region (FSR) to be at $(a, q) = (0.28, 0.7)$ instead of the standard $(0.23, 0.7)$, indicating a modified stability region. According to standard quadrupole theory, the device resolution should be proportional to n^2 , where n is the number of r.f. cycles an ion spends in the QMF [6]. Fig.6 shows data for the ultimate resolution as a function of n^2 . The linear data fit showed a slope of $\sim 1/2$, indicating resolution varying almost linearly with n . This deviation can be partially explained by the results of Dawson [6] and Titov [12]. They report that there is a maximum n where constructional misalignments begin to add up in the ion trajectories, resulting in deviations from the expected dependence. By extension, it is very likely that the higher-order field components of our square geometry introduce a consistently large amount of non-idealities that prevents the device from achieving the conventional frequency dependence.

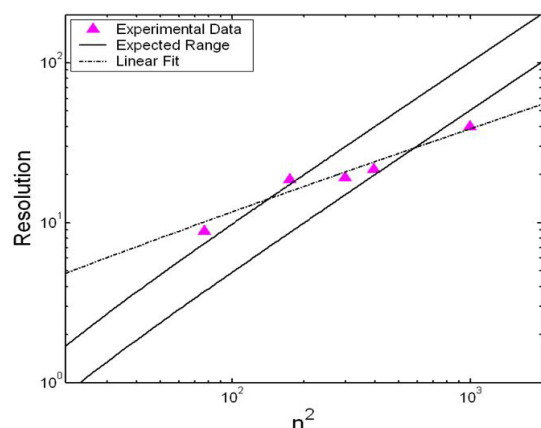


Figure 6. Experimental data plotted with the expected dependence $R = n^2/h$ (solid) for the reported range of h in the first stability region [6].

CONCLUSIONS

In this work, we demonstrated a dynamic range that has more than doubled, a maximum resolution that has increased by a factor of two, and functional ion optics. The new stability diagram observed and the linear dependence on n for resolution suggests new ion dynamics that requires further investigation. Overall, our new class of chip-scale QMFs presents several distinct advantages over other MEMS-based QMF technologies, paving the way for palm portable mass spectrometers.

ACKNOWLEDGEMENTS

The authors would like to thank Dr. Randall Pedder (Ardara Technologies) for his guidance in the device characterization and experimental setup. This work was sponsored by DARPA/MTO and the US Army Soldier Systems Center (Natick, MA) through contract # W911QY-05-1-0002 (DARPA program managers Clark Nguyen and Dennis Polla, and Army program manager Henry Girolamo).

REFERENCES

- [1] E. R. Badman et al., *J. Mass Spec.*, vol. 35, pp. 659-671, 2000.
- [2] S. Boumsellek et al., *J. Am. Soc. for Mass Spec.*, vol. 12, pp. 633-640, 2001.
- [3] R. R. A. Syms, *Anal. and Bioanal. Chem.*, vol. 393, pp. 427-429, 2009.
- [4] L. F. Velásquez-García, et al., in *Tech. Digest of Transducers*, Denver, CO, June 2009, pp. 1646-1649.
- [5] P. S. Riehl, et al., *J. of Microelectromech. Syst.*, vol. 12, no. 5, pp. 577-589, 2003.
- [6] P. Dawson, *Quadrupole Mass Spectrometry and Its Applications*, AIP, New York, 1997.
- [7] S. Taylor et al., *J. Vac. Sci. Technol. B*, vol. 19, no. 2, pp. 557-562, 2001.
- [8] L. F. Velásquez-García et al., *J. Microelectromech. Syst.*, vol. 17, no. 6, pp. 1430-1438, Dec. 2008.
- [9] S. Wright, et al., *J. Am. Soc. for Mass Spec.*, vol. 20, pp. 146-156, 2009.
- [10] K. Cheung, et al., *Tech. Digest Hilton Head Conference*, Hilton Head Island, SC, June 2008, pp. 316-319.
- [11] D.R. Denison, *J. Vac. Sci. Technol. B*, Vol. 8, No. 1, pp. 266-269, 1971.
- [12] V. V. Titov, *J. Am. Soc. for Mass Spec.*, vol. 9, pp. 70-87, 1998.

CONTACT

* Kerry Cheung, cheung@mit.edu